

# The *Infinity-loop microresonator*: a new integrated photonic structure working at an exceptional point

Riccardo Franchi,<sup>1,\*</sup> Stefano Biasi,<sup>1</sup> Diego Piciocchi,<sup>1</sup> and Lorenzo Pavesi<sup>1</sup>

<sup>1</sup>*Nanoscience Laboratory, Department of Physics, University of Trento, 38123 Trento, Italy*

(Dated: February 3, 2023)

Exceptional points, where eigenvalues and eigenvectors coalesce, impact the behavior of different photonics components which show, e.g., enhanced sensing, coherent perfect absorption, unidirectional lasing, and chirality. However, only a few passive geometries have been developed that work on these points. Here, we introduce a novel non-Hermitian structure based on an infinity-shaped microresonator twice coupled to a bus waveguide: the Infinity-Loop Microresonator. Unlike other structures working at an exceptional point, such as a taiji microresonator, the infinity-loop microresonator can achieve either high-contrast or low-contrast unidirectional reflection with a negligible or identical reflection for counterpropagating light. It allows an easy walking through the Riemann sheet by simply controlling the phase of the light propagating in the bus waveguide which makes it a tunable component to build more complex topological structures. Furthermore, the infinity-loop microresonator allows sensors which show the features of both an exceptional point device and a diabolic point device simultaneously.

Keywords: Non-Hermitian microresonator, integrated photonics, exceptional point, microresonators, two-level systems

## I. INTRODUCTION

Non-Hermitian systems have found increasing interest in recent years since they describe open systems such as the one of a propagating optical field in a waveguide [1–4]. Non-Hermitian degenerations in which the eigenvalues and eigenvectors of the system coalesce characterize the physics of exceptional points (EPs) [5–20]. This differs from the physics of Diabolic Points (DPs) which characterize the degeneracy of Hermitian systems where the eigenvalues coalesce while the eigenvectors remain orthogonal. In addition, EPs are of practical interest for different applications such as: enhanced sensors [2, 21–25], unidirectional lasing [26–29], laser line-width broadening [30], chiral transmission [26, 31–35], unidirectional reflection [36], loss-induced transmission [37], unidirectional invisibility [38, 39], topological energy transfer [40], and the breaking of the Lorentz reciprocity theorem [41–43].

A suitable platform to study EPs is integrated optics because of the easy tunability of optical structures as well as the easy realization of non-Hermitian systems that are stable over time. This has led to the realization of various miniaturized optical structures working at an EP, for example: a silicon dioxide (silica) micro-toroid cavity with two silica nano-tips [21], the taiji microresonator [36, 44], two microresonators coupled together and with two bus waveguides [45], a microresonator coupled to a waveguide with at one of the ends a tuneable symmetric reflector [34]. Integrated optical microresonators are particularly appealing since they can be described by a two-level Hamiltonian with propagating and counter-propagating (or clockwise and counterclockwise) optical

modes as eigenstates [46]. Indeed, non-symmetrical microresonators have been used to investigate characteristic phenomena arising from the degeneration of their eigenstates. In fact, the EP degeneration causes these systems to have additional properties and advantages over those of a simple symmetrical microresonator: for example, the enhanced sensing or the unidirectional reflectivity. The geometrical asymmetry allows them to work at an EP resulting in a spectral transmission or reflection response characterized by a single peak or dip. This spectral response is a consequence of the coalescence and, thus, the degeneracy of the eigenvalues.

In this work, we propose a new structure, called the Infinity-Loop Microresonator (ILMR), which although it works at an EP can be geometrically symmetrical and shows resonance splitting in the spectral response. The ILMR is made by an infinity-shaped microresonator and a bus waveguide coupled to both of its lobes (Fig. 1). This peculiar geometrical shape allows preserving the spectral splitting at degeneracy and introduces other characteristic features that make this microresonator suitable for studying the physics of EP and exploiting its properties, e.g. in sensing local perturbations. In Sec. II, we model the ILMR, we demonstrate that it works at an EP and we show that it can be easily tuned to achieve a desired spectral response. Moreover, we analyze how the ILMR behaves under perturbations of its fundamental state. We do not only compute the Riemann sheets related directly to the eigenvalues of the system [1, 3, 8, 10, 47, 48], but we also compute the Riemann sheets from the spectral responses (i.e. the actual observable of the system). In Sec. III, we compare experimental measurements of few structures realized on the silicon photonics platform with the modeling. Here, it is shown that the introduced Temporal Coupled Mode Theory (TCMT) equations faithfully describe the exper-

\* Corresponding author: riccardo.franchi@unitn.it

imental spectral responses and allow quantitatively extracting the relevant parameters of the ILMR. In Sec. IV we compare the ILMR with different types of integrated microresonators, emphasizing the advantages of ILMR in different applications such as in sensing. Sec. V summarizes the paper.

## II. DESIGN AND THEORETICAL MODEL

The ILMR consists of a bus waveguide coupled to an infinity-shaped microresonator formed by two lobes joined together by a crossing (see Fig. 1). As shown in Fig. 1, both the lobes are coupled to the bus waveguide. In addition, the crossing is ideal: the optical mode can only travel through it in a straight line and no excitation of the mode in the cross waveguide is possible (i. e. zero insertion losses and zero cross-talk). In the following, we assume that all the waveguides are single-mode. The relevant parameters of the ILMR are: the resonance frequency ( $\omega_0$ ), the two coupling rates between the lobes and the bus waveguide ( $\Gamma_L$  and  $\Gamma_R$ ), the total loss rate ( $\gamma_{\text{tot}} = \gamma + \Gamma_L + \Gamma_R$ ) and the phase acquired by the optical mode which propagates in the bus waveguide between the two lobes of the infinity-shaped microresonator ( $\varphi$ ). Note that we use the index R,L with reference to left and right in Fig. 1.

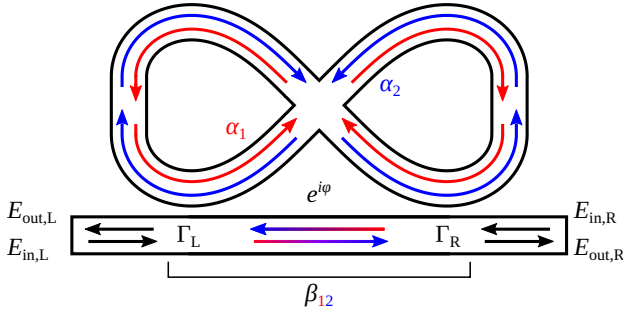


FIG. 1. Sketch of the Infinity-Loop Microresonator (ILMR). All the symbols are described in the main text.

As in a ring microresonator, the ILMR supports two counterpropagating optical modes:  $\alpha_1$  and  $\alpha_2$ . The former,  $\alpha_1$ , is characterized by an electromagnetic wave, which, whenever it transits near the coupling region with the bus waveguide, it is directed toward the center of the microresonator, namely, toward the crossing. While the latter mode,  $\alpha_2$ , travels through the ILMR in the opposite direction, see Fig. 1. As a result, these two modes interact differently with the bus waveguide. First of all, when an optical signal is coupled to the bus waveguide,  $\alpha_1$  is excited first and, then,  $\alpha_2$ . And this happens independently of the excitation direction (i.e. whether the signal is input from the left bus waveguide edge or from the right bus waveguide edge). More importantly, only  $\alpha_1$  can exchange energy with  $\alpha_2$  by means of the bus waveguide. In fact, when  $\alpha_1$  couples to the bus waveguide

it propagates to the other coupling region and excites  $\alpha_2$ . On the contrary, when  $\alpha_2$  couples to the bus waveguide, it can only propagate outward from the microresonator. Consequently, the coupling coefficient ( $\beta_{12}$ ) which links  $\alpha_1$  to  $\alpha_2$  is different from zero ( $\beta_{12} \neq 0$ ) while the coupling coefficient  $\beta_{21}$  which links  $\alpha_2$  to  $\alpha_1$  is 0. Consequently, we can immediately claim that this simple structure works at an EP because it exhibits a completely asymmetric coupling between the two modes ( $\beta_{12} \neq 0$  and  $\beta_{21} = 0$ ).

In order to demonstrate rigorously that the ILMR works at an EP, we model an ideal ILMR, i. e. we neglect any waveguide surface-wall roughness that causing backscattering couples the two counterpropagating modes. By assuming that the ILMR works in the linear regime, i.e. low input optical intensities,  $|E_{\text{in}}|^2 \ll 1 \text{ mW} \cdot \text{Hz}$ , and  $\omega_0 \gg \gamma_{\text{tot}}$ , we can use the Temporal Coupled Mode Theory (TCMT) to describe the system as:

$$i \frac{d}{dt} \begin{pmatrix} \alpha_2 \\ \alpha_1 \end{pmatrix} = \begin{pmatrix} \omega_0 - i\gamma_{\text{tot}} & -i\beta_{12} \\ 0 & \omega_0 - i\gamma_{\text{tot}} \end{pmatrix} \begin{pmatrix} \alpha_2 \\ \alpha_1 \end{pmatrix} - \begin{pmatrix} \sqrt{2\Gamma_R}e^{i\varphi} & \sqrt{2\Gamma_L}e^{i\varphi} \\ \sqrt{2\Gamma_L} & \sqrt{2\Gamma_R} \end{pmatrix} \begin{pmatrix} E_{\text{in,L}} \\ E_{\text{in,R}} \end{pmatrix}, \quad (1)$$

where the coupling between  $\alpha_1$  and  $\alpha_2$  reduces to  $\beta_{12} = 4e^{i\varphi}\sqrt{\Gamma_L\Gamma_R}$ . An alternative way to model this system is to use the Transfer Matrix Method (TMM), see Appendix B. Equation (1) shows that the Hamiltonian of the system is non-Hermitian and, in particular, is equivalent to that of other systems working at an EP, such as the Taiji microresonator [25, 36, 44]. Moreover, the eigenvalues and eigenvectors of the ILMR coalesce:

$$\lambda_1 = \lambda_2 = \omega_0 - i\gamma_{\text{tot}}, \quad \nu_1 = \nu_2 = \begin{pmatrix} 1 \\ 0 \end{pmatrix}. \quad (2)$$

Noteworthy, Eq. (1) and Eq. (2) state that ILMR is respectively a non-Hermitian system and works at an EP.

The output electric fields ( $E_{\text{out,R}}, E_{\text{out,L}}$ ) are related to the input ones ( $E_{\text{in,L}}, E_{\text{in,R}}$ ) and the internal modes of the ILMR in the following way:

$$\begin{pmatrix} E_{\text{out,R}} \\ E_{\text{out,L}} \end{pmatrix} = e^{i\varphi} \begin{pmatrix} E_{\text{in,L}} \\ E_{\text{in,R}} \end{pmatrix} + i \begin{pmatrix} \sqrt{2\Gamma_R} & \sqrt{2\Gamma_L}e^{i\varphi} \\ \sqrt{2\Gamma_L} & \sqrt{2\Gamma_R}e^{i\varphi} \end{pmatrix} \begin{pmatrix} \alpha_2 \\ \alpha_1 \end{pmatrix}. \quad (3)$$

Solving Eq. (1) and Eq. (3) in the steady state and assuming  $E_{\text{in,L}} := \varepsilon_{\text{in,L}}e^{-i\omega t}$ ,  $E_{\text{in,R}} := \varepsilon_{\text{in,R}}e^{i\phi}e^{-i\omega t}$  and  $\alpha_{1/2} := a_{1/2}e^{-i\omega t}$ , we obtain:

$$\varepsilon_{\text{out,R}} = e^{i\varphi} \left( 1 - \frac{2(\Gamma_L + \Gamma_R)}{\gamma_{\text{tot}} - i\Delta\omega} + \frac{8\Gamma_L\Gamma_R}{(\gamma_{\text{tot}} - i\Delta\omega)^2} \right) \varepsilon_{\text{in,L}} - \frac{4e^{i\varphi}\sqrt{\Gamma_L\Gamma_R}}{\gamma_{\text{tot}} - i\Delta\omega} \left( 1 - \frac{2\Gamma_R}{\gamma_{\text{tot}} - i\Delta\omega} \right) \varepsilon_{\text{in,R}}e^{i\phi} \quad (4)$$

$$\varepsilon_{\text{out,L}} = e^{i\varphi} \left( 1 - \frac{2(\Gamma_L + \Gamma_R)}{\gamma_{\text{tot}} - i\Delta\omega} + \frac{8\Gamma_L\Gamma_R}{(\gamma_{\text{tot}} - i\Delta\omega)^2} \right) \varepsilon_{\text{in,R}}e^{i\phi} - \frac{4e^{i\varphi}\sqrt{\Gamma_L\Gamma_R}}{\gamma_{\text{tot}} - i\Delta\omega} \left( 1 - \frac{2\Gamma_L}{\gamma_{\text{tot}} - i\Delta\omega} \right) \varepsilon_{\text{in,L}}, \quad (5)$$

where  $\Delta\omega = \omega - \omega_0$ . Equation (4) and Eq. (5) can also be used in an interferometric excitation [44, 49], where the system is simultaneously excited from both the input ports with two coherent electromagnetic fields out of phase by  $\phi$ . To derive the formulas for a single side excitation, it is sufficient to impose  $\varepsilon_{\text{in,R}}$  or  $\varepsilon_{\text{in,L}}$  equal to zero. Equation (4) and Eq. (5) show that the intensities of the output fields do not depend on the phase acquired in the bus waveguide between the two lobes of the ILMR, in fact, the term  $e^{i\varphi}$  can be collected. This means that it is possible to change the phase of the coefficient  $\beta_{12} = 4e^{i\varphi}\sqrt{\Gamma_L\Gamma_R}$  without changing the response of the ideal ILMR.

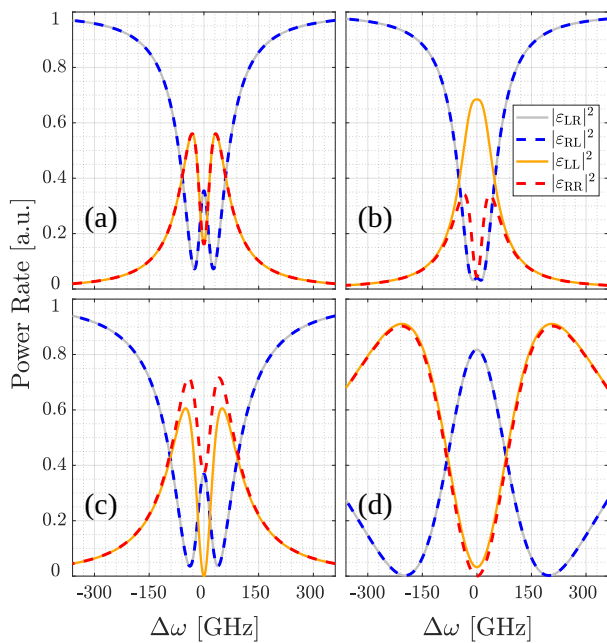


FIG. 2. Spectral response of four different ILMR: (a) a symmetric ILMR characterized by the same coupling coefficients ( $\Gamma_L = \Gamma_R$ ) and (b), (c) and (d) an asymmetric ILMR with different coupling coefficients ( $\Gamma_L \neq \Gamma_R$ ). Solid lines identify the spectral responses of the system when it is excited from the left side of the bus waveguide, while dashed lines identify those related to excitation from right. Gray and blue lines refer to transmission spectra, while orange and red lines refer to reflection spectra. The used parameters are the nominal ones for the fabricated ILMRs and are reported in Table I in Appendix A.

Figure 2 reports the single excitation response of four different designed ILMR: (a) symmetric ILMR and (b), (c), (d) asymmetric ILMR. Here, with symmetric and asymmetric we mean ILMR with the same coupling coefficients ( $\Gamma_L = \Gamma_R$ ) or with two different coupling coefficients ( $\Gamma_L \neq \Gamma_R$ ), respectively. For more information about the used parameters see Table I in Appendix A. In the following, we identify the field intensity at the  $j$  output when the device is excited from the  $i$  input as  $|\varepsilon_{ij}|^2$ , where  $i = L, R$  and  $j = L, R$  (L stands for Left and R

stands for Right). Figure 2 (a) reports counterintuitive transmissions and reflections. In fact, since the ILMR works at an EP, one would expect that the transmission and reflection spectra would be characterized by a single dip and peak (coincident eigenvalues), respectively. Here, however, we do observe a doublet characterized by two dips and peaks having the same extinction rate. Note that this splitting is not due to the spurious coupling caused by backscattering [46], but it is due to the interference of the different electric fields at the output, see Eq. (4) and Eq. (5). It also emphasizes that the positions of minima in transmission are not the eigenvalues of the cavity under analysis.

By varying the coupling rates between the bus waveguide and the lobes of the ILMR ( $\Gamma_L$  and  $\Gamma_R$ ), one can obtain different spectral responses. Particularly, in Fig. 2 (b), the transmission spectrum shows a quasi-negligible splitting, as well as in the reflection from the left side of the bus waveguide ( $|\varepsilon_{LL}|^2$ ). Differently, the reflection from the opposite side ( $|\varepsilon_{RR}|^2$ ) exhibits a clear doublet. Moreover, in resonance, the two reflections are completely different reaching a ratio of  $|\varepsilon_{LL}|^2/|\varepsilon_{RR}|^2 \simeq 15$ . By further varying the parameters  $\Gamma_L$  and  $\Gamma_R$  asymmetrically, one finds the spectral response reported in Fig. 2 (c). Here, the reflection  $|\varepsilon_{LL}|^2$ , at the resonance frequency ( $\Delta\omega = 0$ ), reduces to zero. These different spectral response demonstrates the potential of the ILMR. Interestingly, the relation between the parameters which yield this spectral response is easily calculated via Eq. (4). Imposing  $|\varepsilon_{\text{in,R}}|^2 = 0$  and  $|\varepsilon_{\text{out,L}}|^2 = 0$ , at  $\Delta\omega = 0$ , gives:  $2\Gamma_L = \gamma_{\text{tot}}$  and then  $\Gamma_L = \Gamma_R + \gamma$ . Through the increase of  $\Gamma_L$  and  $\Gamma_R$  of the ILMR, it is also possible to exchange the transmission spectrum with the reflection spectrum by obtaining a peak in transmission and a dip in reflection at resonance, see Fig. 2 (d). Noteworthy, these different spectral responses are obtained while remaining on an EP.

### A. Backscattering and Sensing

An integrated microresonator having high quality factor exhibits spurious backscattering mainly due to the surface roughness of the waveguides. The presence of this backscattering causes coupling between the counter-propagating modes of the microresonator, in our case  $\alpha_1$  and  $\alpha_2$ . To include this phenomenon in our theory, we need to add to the model of the ideal ILMR Eq. (1) the following term:

$$\begin{pmatrix} 0 & -i\beta_{\text{Bs},12} \\ -i\beta_{\text{Bs},21} & 0 \end{pmatrix} \begin{pmatrix} \alpha_2 \\ \alpha_1 \end{pmatrix}, \quad (6)$$

where  $\beta_{\text{Bs},12}$  and  $\beta_{\text{Bs},21}$  are the backscattering coefficients that induce the spurious coupling between  $\alpha_1$  and  $\alpha_2$ . Consequently, the Hamiltonian of the system results to:

$$\mathcal{H} = \begin{pmatrix} \omega_0 - i\gamma_{\text{tot}} & -i(\beta_{12} + \beta_{\text{Bs},12}) \\ -i\beta_{\text{Bs},21} & \omega_0 - i\gamma_{\text{tot}} \end{pmatrix}. \quad (7)$$

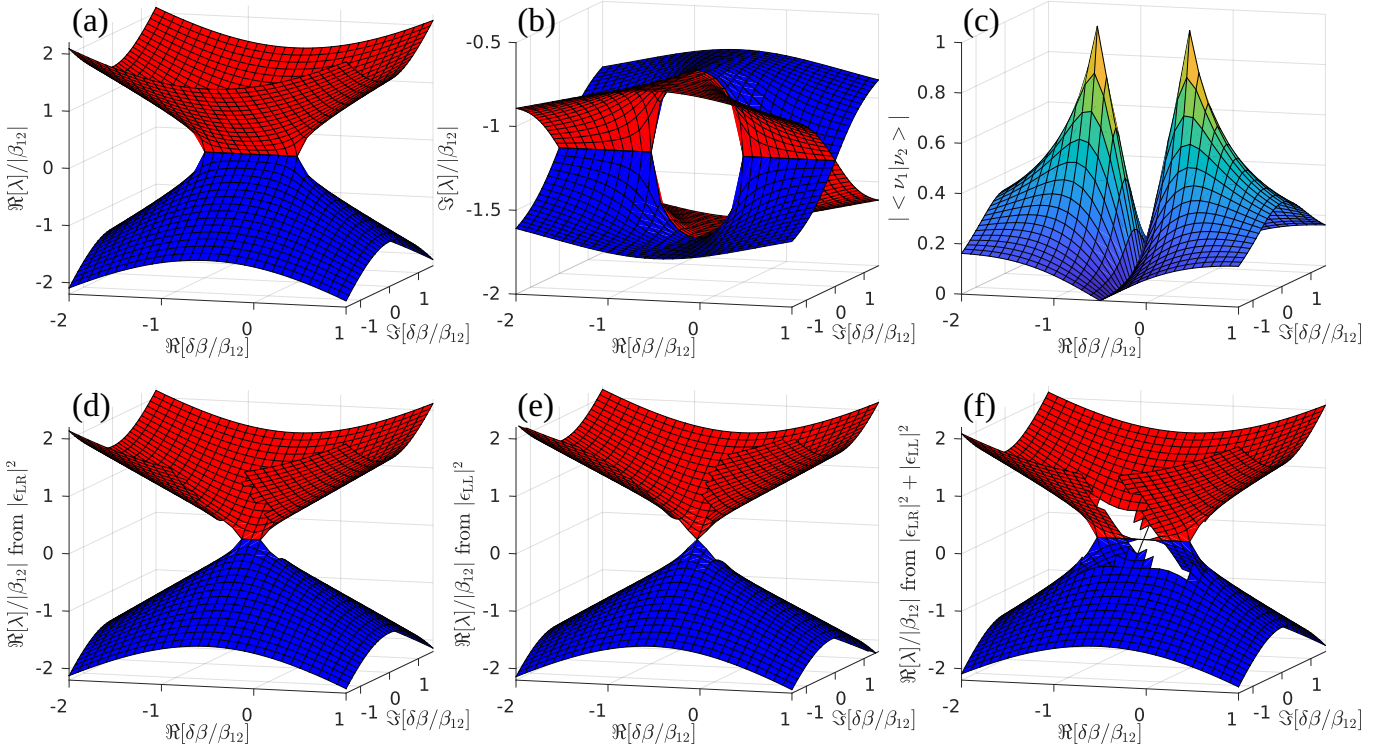


FIG. 3. Normalized Riemann sheets for the ILMR as a function of the real  $\Re[\delta\beta]$  and the imaginary  $\Im[\delta\beta]$  part of the hermitian backscattering perturbation ( $\delta\beta$ ). All the quantities are normalized to  $\beta_{12}$ . (a) and (b) report the maps of the real  $\Re[\lambda]$  and of the imaginary  $\Im[\lambda]$  parts of the eigenvalues. The red and blue surfaces refer to the first ( $\lambda_1$ ) and the second ( $\lambda_2$ ) eigenvalue, respectively. (c) shows the map of the absolute value of the inner product between the two eigenvectors ( $|\langle \nu_1 | \nu_2 \rangle|$ ). (d), (e) and (f) represent the map of the positions of the spectra minima for (d) and (f) and maxima for (e) of the transmission ( $|\varepsilon_{LR}|^2$ ), reflection ( $|\varepsilon_{LL}|^2$ ) and the sum of the two ( $|\varepsilon_{LR}|^2 + |\varepsilon_{LL}|^2$ ), respectively. The holes in panels (d), (e), and (f) are due to the inability to recognize two peaks. Here, we use  $\Gamma_L = \Gamma_R = 1/4[\text{a.u.}]$  to get  $\beta_{12} = 1[\text{a.u.}]$  and  $\gamma = \Gamma_L$ . Division by  $\beta_{12}$  or its modulus was done to make the graphs independent of the relative phase between  $\delta\beta$  and  $\beta_{12}$  and of the absolute value of  $\beta_{12}$ .

As a result, the eigenvalues and eigenvectors no longer coalesce, but are:

$$\lambda_{1/2} = \omega_0 \pm \sqrt{-(\beta_{12} + \beta_{Bs,12})\beta_{Bs,21}} - i\gamma_{tot} \Rightarrow \lambda_1 \neq \lambda_2 \quad (8)$$

$$\nu_{1/2} = \frac{1}{\sqrt{\langle \nu_{1/2} | \nu_{1/2} \rangle}} \left( \mp \frac{\sqrt{(\beta_{12} + \beta_{Bs,12})\beta_{Bs,21}}}{\beta_{Bs,21}} \right) \Rightarrow \nu_1 \not\parallel \nu_2. \quad (9)$$

Usually backscattering, related for example to surface roughness, can be considered as a Hermitian perturbation to the ideal Hamiltonian, where  $\delta\beta := \beta_{Bs,12} = -\beta_{Bs,21}^*$ . Generalizing, we can consider this perturbation not only due to the surface-wall roughness but also due to any molecules/substances in the waveguide cladding. Therefore,  $\delta\beta$  can simply be interpreted as the perturbation that we want to probe with an ILMR based optical sensor.

To determine the sensing potential of the ILMR toward a  $\delta\beta$  perturbation, we assume that ideally both the real and imaginary parts of the eigenvalues can be

measured. Figure 3 (a) and (b) show the computed real and the imaginary parts of the eigenvalues divided by  $|\beta_{12}|$  as a function of  $\Re[\delta\beta/\beta_{12}]$  and  $\Im[\delta\beta/\beta_{12}]$ . Here, the two eigenvalues are shown with the red and blue surfaces (Riemann sheets [2, 3, 48]). Fig. 3 (a) shows that the real part of the two eigenvalues are equal when  $\Im[\delta\beta/\beta_{12}] = 0$  and  $-1 \leq \Re[\delta\beta/\beta_{12}] \leq 0$ , at the same time Fig. 3 (b) shows that the imaginary part of the two eigenvalues are equal when  $\Im[\delta\beta/\beta_{12}] = 0$  and  $\Re[\delta\beta/\beta_{12}] \leq -1 \vee \Re[\delta\beta/\beta_{12}] \geq 0$ . In addition, Fig. 3 (c) shows that only at (0,0) and at (-1,0) the inner product of the two eigenvectors,  $|\langle \nu_1 | \nu_2 \rangle|$ , is equal to one. As a result, starting from the ideal ILMR at (0,0), we can reach another EP by varying the perturbation  $\delta\beta$  in order to reach the point (-1,0). Moreover, Fig. 3 shows that only the Riemann sheets in (b) are intersected, while in (a) they are not.

As already discussed, the coefficient  $\beta_{12}$  is equal to  $4e^{i\varphi}\sqrt{\Gamma_L\Gamma_R}$ , where  $e^{i\varphi}$  is the acquired phase that the mode acquires by going from one lobe to the other through the bus waveguide. This means that by varying  $\varphi$ , for example by means of a phase shifter component integrated in the bus waveguide, one is able to vary the

eigenvalues of the system along a circular path with respect to the EP within the same perturbation  $\delta\beta$ . This encircling of the EP follows the Riemann sheets given in Fig. 3. In this way, we would be able to align  $\beta_{12}$  with  $\delta\beta$ , thus being able to vary the spectral sensitivity of the ILMR to this perturbation. Consequently, the variation of  $\varphi$  increases the difference between the real part of the eigenvalues by causing  $\Im[\delta\beta/\beta_{12}] = 0 \wedge \Re[\delta\beta/\beta_{12}] > 0$ . Furthermore, thanks to this interesting feature, ILMR can be used to study the dynamic encircling of an EP as in [8, 10].

To derive the real part  $\Re[\lambda]$  of the eigenvalues, from the spectral responses of the system, it is customary to compute the spectral position of the two minima of the Autler-Townes splitting doublet [21, 50]. However, as we already pointed out, the frequencies of the minima of the dips in the transmission spectrum do not give the eigenvalues. In fact, at an EP the eigenvalues are equal while, as shown in Fig. 2 (a), the transmission and reflection of an ILMR exhibit a resonant doublet. Therefore to use the ILMR as a sensor, let us consider a symmetric ILMR having  $\Gamma_L = \Gamma_R = 1/4$  [a.u.] and  $\gamma = \Gamma_{L/R}$ . In this case, the normalized spectral minima or maxima for the transmitted power ( $|\varepsilon_{LR}|^2$ ), the reflected power ( $|\varepsilon_{LL}|^2$ ), and for the sum of the two ( $|\varepsilon_{LR}|^2 + |\varepsilon_{LL}|^2$ ) are shown in Fig. 3 (d), (e) and (f), respectively. The spectrum of  $|\varepsilon_{LR}|^2 + |\varepsilon_{LL}|^2$  yields the frequencies where the system has greater losses, which interestingly have a good correspondence with the eigenvalues of the system, as can be seen by comparing Fig. 3 (a) and (f). In Fig. 3 (d), (e) and (f) there are regions in which the Riemann sheets are not defined, and therefore, show a hole. In these regions, there is either only one non-zero peak in the spectrum or the second peak is masked by the first one. Finally, by simultaneously being able to measure the splitting relative to all the three spectra, and also by being able to encircle an EP, it is possible to improve the accuracy in the  $\delta\beta$  perturbation sensing.

This last conclusion is evidenced by looking at the splitting ( $\Re[\Delta\lambda]/|\beta_{12}|$ ) as a function of  $\Re[\delta\beta/\beta_{12}]$  by imposing  $\Im[\delta\beta/\beta_{12}] = 0$  (Fig. 4). In fact, by comparing Fig. 4 (a) and (b), we observe that the doublet is replaced by a single dip in the spectrum of the sum of the transmission and reflection of the ideal ILMR. Furthermore, Fig. 4 (c) shows that the actual splitting of the eigenvalues  $\Re[\Delta\lambda]$  is well represented by the splitting in the spectrum of  $|\varepsilon_{LR}|^2 + |\varepsilon_{LL}|^2$ , as also shown in Fig. 3 (a) and (f). As can also be derived from Eq. (8), for small perturbations  $\delta\beta$ , the splitting follows the square-root characteristic of EPs [21, 22, 25]. Fig. 4 (c) shows that, for  $\delta\beta$  around and greater than zero, both the splittings in the transmission spectra and in the reflection spectra vary linearly as a function of the perturbation. Therefore, by using the ILMR one is able to simultaneously use both the enhanced sensing of the EP due to the square root dependence as well as the linear dependence, which can be very useful during sensor calibration. Moreover, we observe that the latter, by covering the part near  $\delta\beta = 0$ ,

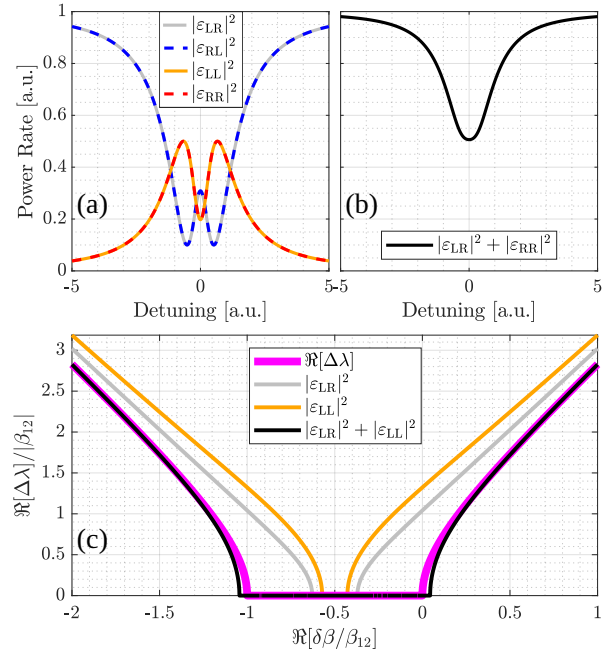


FIG. 4. Output spectra of a symmetric ILMR ( $\Gamma_L = \Gamma_R$ ). (a) shows the different transmission and reflection spectra for left or right excitation. (b) reports the sum of the output field intensities at the right (transmission) and left (reflection) ports when the ILMR is excited from left ( $|\varepsilon_{LR}|^2 + |\varepsilon_{LL}|^2$ ). (c) represents with different colors the splitting of the eigenvalues or the doublets observed in the spectra of  $|\varepsilon_{LR}|^2$ ,  $|\varepsilon_{LL}|^2$  and  $|\varepsilon_{LR}|^2 + |\varepsilon_{LL}|^2$  as a function of the backscattering perturbation  $\delta\beta/\beta_{12}$ . Here we use  $\Gamma_L = \Gamma_R = 1/4$  [a.u.] to get  $\beta_{12} = 1$  [a.u.] and  $\gamma = \Gamma_L$ .

enlarges the working region of the sensor.

### III. EXPERIMENTAL MEASUREMENTS

#### A. Experimental setup and samples

To verify the theoretical prediction we have designed four different ILMRs: one symmetric ( $\Gamma_L = \Gamma_R$ ) and the others asymmetric ( $\Gamma_L \neq \Gamma_R$ ), see Fig. 5. These have been fabricated with  $450 \text{ nm} \times 220 \text{ nm}$  cross section silicon waveguides embedded in a silica cladding by the IMEC/Europractice facility within a multi-project wafer program.

The symmetrical ILMR geometry is characterized by a crossing, four  $3\pi/4$  Euler curves with a minimum radius of  $15 \mu\text{m}$ , point coupling regions and straight waveguides to connect the various elements and draw the bus waveguide. The gap widths between the loops and the bus waveguide are  $165 \text{ nm}$ . The crossings used are those of the design kit of the IMEC/Europractice facility, which from our measurements at  $1550 \text{ nm}$  have losses of

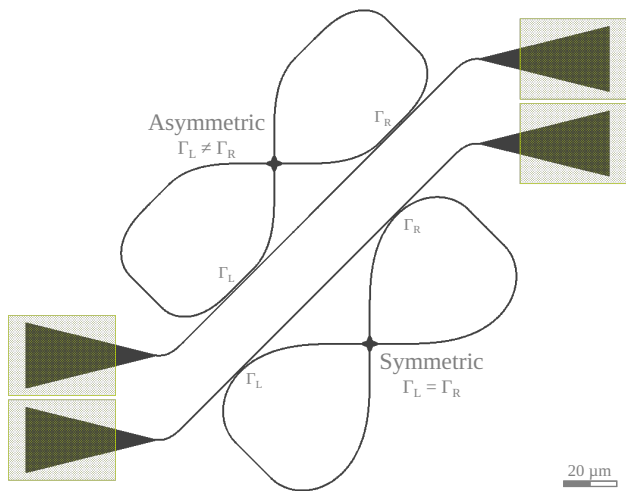


FIG. 5. The design of an asymmetric (top) and a symmetric (bottom) ILMRs. The silicon waveguides are indicated by the black lines. The yellow boxes identify the input/output grating regions.

$0.18 \pm 0.01$  dB/crossing and negligible reflections. The asymmetric ILMR geometry has straight coupling regions (length  $\simeq 10 \mu\text{m}$ ) and gaps which differ for the various asymmetric geometries  $\text{gap}_L = [392, 288, 205]$  nm and  $\text{gap}_R = [300, 326, 198]$  nm. In addition, the loops are achieved with Euler curves with a minimum radius equal to  $10 \mu\text{m}$ .

The ILMRs were measured by using an interferometric optical setup [44]. It allows simultaneous measurement of transmission and reflection in both the excitation directions. Briefly, the set-up is based on a Continuous-Wave tunable laser whose output beam is divided by a fiber splitter into two arms. These arms contain a Variable Optical Attenuator (VOA), a fiber polarization controller, and an optical circulator with one of its outputs connected to an InGaAs photodetector. Both arms end on a stripped fiber that couples light to the sample. We used a laser wavelength around  $1.55 \mu\text{m}$  and a power of about  $10 \mu\text{W}$ .

## B. Results

The spectral response of the four different ILMRs were measured for both excitation directions (Fig. 6). The transmission and reflection spectra from both side are plotted with gray/blue and orange/red lines, respectively. In particular, the gray and orange lines correspond to an input excitation from the left while the blue and red lines from the right. The dashed black lines refer to the fit of the spectra by the theory of the previous section which were performed on the four spectral responses with the same parameters (fit parameters are reported in Table II of Appendix A).

As expected, four different types of spectral responses

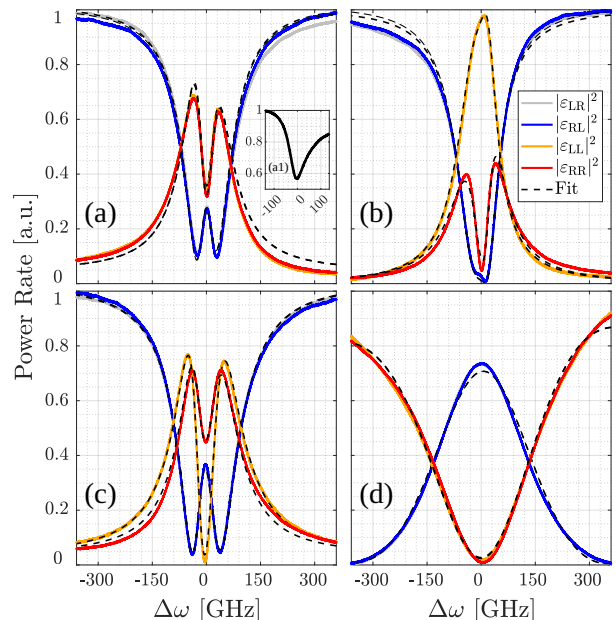


FIG. 6. Experimental spectra of four different ILMRs. The dashed black lines identify the fits with the Temporal Coupled Mode Theory equations. The solid lines represent the experimental data. In gray and blue lines are reported the transmission spectra while in orange and red lines are reported the reflection spectra. Moreover, the gray and orange lines correspond to an input excitation from the left while the blue and red lines from the right. The inset (a1) shows the sum of the transmitted and reflected intensities, when the ILMR is excited from left ( $|\varepsilon_{LR}|^2 + |\varepsilon_{LL}|^2$ ).

are observed in Fig. 6. Spectra are similar to those reported in Fig. 2. Their asymmetry with respect to a detuning  $\Delta\omega = 0$  is caused by the backscattering induced by the surface-wall roughness. Indeed, the theoretical fit which includes the backscattering matches the experimental data. This validates the modeling given by the system of equations [Eq. (1), Eq. (3), Eq. (6), and Eq. (7)], reported in Sec. II. The fit parameters reported in Table II of Appendix A show that the backscattering is non-Hermitian because  $n := (\beta_{Bs,12} + \beta_{Bs,21}^*)/2 \neq 0$  [44, 46]. As a further check, if we let  $|\beta_{12}|$  run as a free parameter in the fit, we obtain values that are compatible with  $4\sqrt{\Gamma_L\Gamma_R}$ . This also remarks on the validity of our theoretical model.

Figure 6 (a1, inset) shows the sum of the two measured output intensities ( $|\varepsilon_{LR}|^2 + |\varepsilon_{LL}|^2$ ) for a left excitation of the symmetric ILMR. In this spectrum, as expected from the theoretical simulations (Fig. 4), the splitting disappears. Only one minimum is observed at approximately zero detuning (resonance). The asymmetry of the peak is attributed to the presence of the backscattering, which is a non-Hermitian perturbation whose complex vector  $[\beta_{Bs,12}$  in Eq. (7)] does not have the same direction as  $\beta_{12}$ , see Table II of Appendix A.

#### IV. DISCUSSION

In the literature, other microresonator geometries that work at an EP have been demonstrated [21, 25, 34, 36, 45]. The symmetric ILMR differs from all these devices because, although the eigenvalues and eigenvectors coalesce, the spectral responses in transmission and reflection exhibit resonance splitting.

It is interesting to compare more in detail the ILMR and the taiji geometry [36] since they are topological equivalent<sup>1</sup>. In fact, assuming ideal crossings, the ILMR is equivalent to a taiji microresonator excited by the S-shaped waveguide, see Fig. 8 (b) in Appendix B. However, while in the case of a taiji microresonator the bus waveguide is not necessary for the resonator to work at an exceptional point, for the ILMR the bus waveguide is essential. This means that the total losses of the taiji microresonator, having further couplings the bus waveguide for input and output, are higher than those of the ILMR, see Fig. 7 (b). Moreover, it is easy to see that the ILMR is also equivalent to the structure schematized in Fig. 8 (c) in Appendix B, which is characterized by a microring resonator having two couplings with the bus waveguide, and the crossing no longer turns out to be internal to the microring resonator, but between the two couplings in the bus waveguide.

Let us further compare the sensitivity to an external perturbation of the ILMR with those of other types of integrated microresonators. In Fig. 7, we show the ILMR (a), the taiji microresonator (b), and the simple microring resonator (c). Here, we assume the same propagation losses and that the coupling coefficients are equal to the loss rate ( $\gamma_{\text{Ring}} = \gamma_{\text{Taiji}} = \gamma = \Gamma_L$ ,  $\Gamma_{\text{Ring}} = \Gamma_{\text{Taiji}} = \Gamma_S = \Gamma_L = \Gamma_R = 1/4$  [a.u.],  $\beta_{12} = 4e^{i\varphi}\sqrt{\Gamma_L\Gamma_R} = 1$  [a.u.], and  $\beta_{12,\text{Taiji}} = 4e^{i\varphi}\Gamma_S = 1$  [a.u.]). The equations used are given in Appendix C. Figure 7 shows that the eigenvalue splittings for the ILMR and the taiji microresonator follow the expected square-root dependence on small perturbations. The splitting for an EP microresonator is greater than that for a structure working at a diabolic point, such as the simple microresonator. In this last case, a linear trend in splitting versus the perturbation is observed [21, 25]. Although the trend of the eigenvalues is very interesting, it is not easy to access them directly in an experiment; in fact the spectral positions of the transmission minima do not accurately reflect the eigenvalues. Therefore, in order to make a more useful comparison from an application point of view, we have reported the transmission minima splittings obtained from the spectra in Fig. 7.

From the experimentally observable transmission spectra, there is always a region where two distinct minima cannot be observed because the spectral width of the peaks makes them indistinguishable or the noise masks

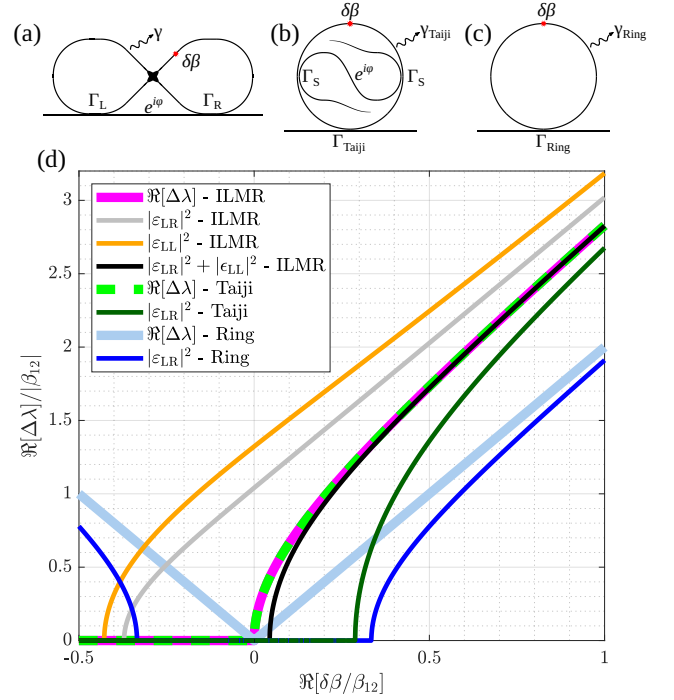


FIG. 7. Splitting of the eigenvalues or doublets present in the spectra as a function of the perturbation  $\delta\beta/\beta_{12}$  for three different structures: an ILMR (a), a taiji microresonator (b) and a microring resonator (c). Here we used  $\Gamma_{\text{Ring}} = \Gamma_{\text{Taiji}} = \Gamma_S = \Gamma_L = \Gamma_R = 1/4$  [a.u.] to get  $\beta_{12} = 1$  [a.u.],  $\beta_{12,\text{Taiji}} = 4e^{i\varphi}\Gamma_S = 1$  [a.u.], and  $\gamma_{\text{Ring}} = \gamma_{\text{Taiji}} = \gamma = \Gamma_L$ . In this figure the conditions  $\Im[\delta\beta/\beta_{12}] = 0$  and  $\delta\beta = \beta_{\text{Bs},12} = -\beta_{\text{Bs},21}^*$  were used. The thick lines represent eigenvalues, while the thin lines represent experimentally measurable quantities.

the splitting [11, 12, 21]. However, by using the ILMR one has the possibility of using not only the sum of the transmitted and the reflected intensity, i.e., the square-root trend, but also the two intensities separately, i.e., the linear trend where the splitting is maintained. By exploiting this characteristic feature of the ILMR, one is also able to use the region around small perturbations where the other structures are unusable because of resolution or noise. Furthermore, it is observed that using  $|\epsilon_{\text{LR}}|^2 + |\epsilon_{\text{LL}}|^2$  in a ILMR one is able to decrease the width of this region, see Fig. 7. In addition, one can vary the phase  $\varphi$  between the two lobes of the ILMR or in the S-shaped waveguide for the taiji microresonator to align  $\beta_{12}$  with the perturbation  $\delta\beta$ , and thus one achieves a maximum splitting in the optical response. Such a condition corresponds to rotate  $\beta_{12}$  so that  $\Re[\delta\beta/\beta_{12}] \geq 0$  and  $\Im[\delta\beta/\beta_{12}] = 0$ . This alignment within the complex plane is easily performed with the ILMR to be compared with the difficulty of tuning nano-tips as in the case of [21]. A last remark is about the role of the crossing in the ILMR, which is one critical element of the proposed geometry. If crossing losses are predominant over other losses, the efficiency in distinguishing small perturbations with the square root trend would decrease, however, the

<sup>1</sup> we thank I. Carusotto for this remark

linear trend still provides a way to detect the perturbation. This is another advantage of the ILMR which makes it robust with respect to imperfections.

## V. CONCLUSIONS

We have proposed a novel integrated photonic microresonator that works at an Exceptional Point (EP): the Infinity-Loop Microresonator (ILMR). This device, consisting of an infinity-shaped waveguide coupled with a bus waveguide at its two lobes, has several interesting features. The ILMR is always on an EP, whatever the two coupling coefficients with the bus waveguide. A symmetric ILMR presents a doublet in the spectral responses. By varying the couplings, different shapes in transmission and reflection with absolute zero reflection or zero transmission at resonance can be obtained. By different side excitation, one can either get identical reflections or completely different reflections. All these features are achieved while keeping the ILMR on an EP.

Furthermore, we have studied the improvements in sensing applications provided by the ILMR which are related to the possibility to observe at the same time both a square-root (sensitivity enhancement) and a linear dependence of the spectral splitting as a function of a Hermitian perturbation. This feature washes out the insensitive region of an EP optical sensor caused by resolution or noise. This last observation strengthens the potential of the ILMR as a device that could exploit both the characteristics of an EP and the linearity of a diabolic point.

The strong spectral asymmetry and the ease of control of the coupling phase between the two lobes via integrated phase shifters make the ILMR a suitable tunable element for more complex geometries where arrays of interconnected ILMR can be used to realize integrated topological structures or to study the EP from a quantum point of view.

### Appendix A: Infinity-Loop Microresonator parameters

In Table I we report all the parameters used in Sec. II. These parameters are those that were derived through simulations of the couplings during the design of the ILMRs.

	$\Gamma_L$ [GHz]	$\Gamma_R$ [GHz]	$\gamma_{\text{tot}}$ [GHz]
Fig. 2 (a)	12.6	12.6	35
Fig. 2 (b)	5.1	21.6	36.5
Fig. 2 (c)	25	15.2	50
Fig. 2 (d)	94.1	104	207.9

TABLE I. Parameters used in Fig. 2 of Sec. II.

The parameters derived through fits of the experimental data in Fig. 6 are listed in Table II.

	Fig. 6 (a)	Fig. 6 (b)	Fig. 6 (c)	Fig. 6 (d)
$\Gamma_L$ [GHz]	12.86(7)	5.81(3)	23.90(6)	183(1)
$\Gamma_R$ [GHz]	13.25(7)	30.8(3)	12.1(1)	182(1)
$\gamma_{\text{tot}}$ [GHz]	39.9(3)	43.7(3)	47.0(3)	400(2)
$ \beta_{12} $ [GHz]	52.2(8)	54(1)	68(1)	732(14)
$\arg[\beta_{12}]$	0.1436(6)	-2.148(3)	-1.865(6)	1.64(1)
$ \beta_{Bs,12} $ [GHz]	2.21(2)	5.90(3)	5.93(6)	18.77(1)
$\arg[\beta_{Bs,12}]$	0.782(7)	1.567(8)	1.85(1)	1.000(9)
$ \beta_{Bs,21} $ [GHz]	3.40(2)	13.1(1)	8.90(8)	23.12(1)
$\arg[\beta_{Bs,21}]$	1.11(1)	0.981(4)	1.047(7)	1.77(1)

TABLE II. Parameters derived through fits of experimental data reported in Fig. 6.

### Appendix B: Transfer Matrix Method

As reported in the main text, the three structures sketched in Fig. 8 are equivalent, as demonstrated by the fact that their optical modes follow the same equations.

In order to describe the ILMR, the Transfer Matrix Method (TMM) can also be used. Using the coefficients given in Fig. 8, where  $t$  are the transmission coefficients of the specific coupling region while  $k$  are the coupling coefficients, we are able to write the following system of equations:

$$E_1 = t_1 E_0 + ik_1 E_9, \quad E_{0r} = t_1 E_{1r} + ik_1 E_{4r}, \quad (B1)$$

$$\begin{aligned} E_2 &= e^{i\varphi} E_1, & E_{1r} &= e^{i\varphi} E_{2r}, \\ E_3 &= t_2 E_2 + ik_2 E_{8r}, & E_{2r} &= t_2 E_{3r} + ik_2 E_7, \\ E_4 &= t_1 E_9 + ik_1 E_0, & E_{4r} &= e^{i\psi_{45}} E_{5r}, \\ E_5 &= e^{i\psi_{45}} E_4, & E_{5r} &= t_{Bs} E_{6r} - b_{Bs,12} E_5, \\ E_6 &= t_{Bs} E_5 - b_{Bs,21} E_{6r}, & E_{6r} &= e^{i\psi_{67}} E_{7r}, \\ E_7 &= e^{i\psi_{67}} E_6, & E_{7r} &= t_2 E_{8r} + ik_2 E_2, \\ E_8 &= t_2 E_7 + ik_2 E_{3r}, & E_{8r} &= e^{i\psi_{89}} E_{9r}, \\ E_9 &= e^{i\psi_{89}} E_8, & E_{9r} &= t_1 E_{4r} + ik_1 E_{1r}, \end{aligned}$$

$$\psi_{jl} = \frac{2\pi}{\lambda} n_{\text{eff}} L_{jl} + i\alpha L_{jl}, \quad L = L_{45} + L_{67} + L_{89},$$

$$\psi = \frac{2\pi}{\lambda} n_{\text{eff}} L + i\alpha L.$$

In the following, for simplicity, we assumed that in the couplings between the bus waveguide and the lobes there are no losses ( $t_{1/2}^2 + k_{1/2}^2 = 1$ ). The parameter  $L_{ij}$  identifies the waveguide length between the numbers  $i$  and  $j$  reported in Fig. 8.  $\varphi$ , as in the main text, is the acquired phase to go from 1 to 2, see Fig. 8. We associated the backscattering with a scatterer (black star



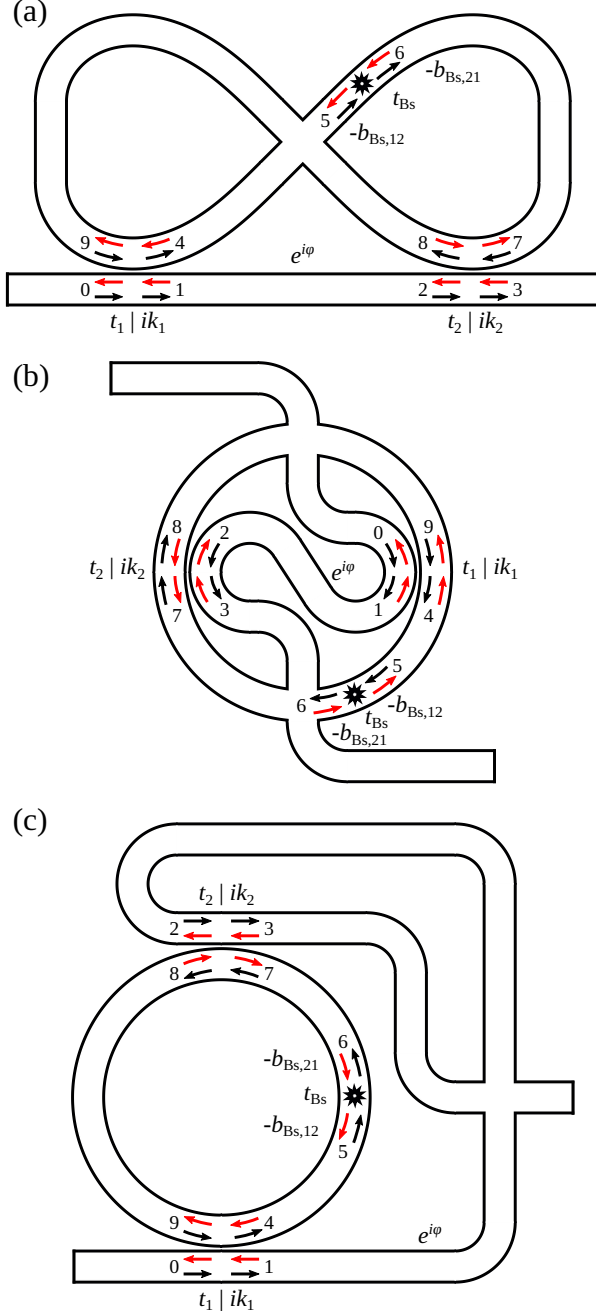


FIG. 8. Sketches of microresonators ideally equal to a ILMR. (a) ILMR, (b) taiji microresonator excited from the S-shaped waveguide, and (c) microresonator having two couplings with the bus waveguide having within it a crossing. The black arrows identify the  $E_n$  fields, with  $n = 0, \dots, 9$ , and their propagation direction. Instead, the red arrows identify the fields  $E_{nr}$ , having opposite propagation directions. All the parameters are described in the text.

in Fig. 8) characterized by the coefficients  $t_{Bs}$ ,  $-b_{Bs,12}$ , and  $-b_{Bs,21}$ . The losses due to the crossing are absorbed either in the propagation losses ( $\alpha$ ) or in the factor  $t_{Bs}$ , while the possible coupling between the counterpropagat-

ing modes given by crossing can be incorporated within the coefficients  $b_{Bs,12}$  and  $b_{Bs,21}$ . To be noted that this crossing cross-talk turns out to be negligible compared with the backscattering given by the surface roughness of the waveguides. From Eq. (B1) we derive:

$$\varepsilon_{LR} = \varepsilon_{RL} = \frac{N}{D}, \quad \varepsilon_{LL} = \frac{N_{LL}}{D}, \quad \varepsilon_{RR} = \frac{N_{RR}}{D} \quad (B2)$$

$$\varepsilon_{out,R} = \varepsilon_{in,L}\varepsilon_{LR} + \varepsilon_{in,R}e^{i\phi}\varepsilon_{RR}, \quad (B3)$$

$$\varepsilon_{out,L} = \varepsilon_{in,R}e^{i\phi}\varepsilon_{RL} + \varepsilon_{in,L}\varepsilon_{LL}. \quad (B4)$$

where

$$N = [(t_2^2 - 2)t_1^2 - 2t_2^2 + 1]t_{Bs}e^{i(\psi+\varphi)} + t_1 \left( k_1 k_2 e^{i(2\psi_{45} + \psi_{89})} b_{Bs,12} + t_2 e^{i\varphi} \right) t_1 e^{i(2\psi_{67} + \psi_{89} + \varphi)} \left[ t_2 e^{i(2\psi_{45} + \psi_{89})} (t_{Bs}^2 - b_{Bs,12}b_{Bs,21}) - k_1 k_2 e^{i\varphi} b_{Bs,21} \right] \quad (B5)$$

$$N_{LL} = 2k_1 k_2 e^{i(\psi_{45} + \psi_{67} + \varphi)} \left[ -t_1 t_{Bs} + t_2 e^{i\psi} (t_{Bs}^2 - b_{Bs,12}b_{Bs,21}) \right] - (t_1^2 - 1) e^{2i\psi_{45}} b_{Bs,12} + (t_2^2 - 1) t_1^2 \left( -e^{2i(\psi_{67} + \varphi)} \right) b_{Bs,21} \quad (B6)$$

$$N_{RR} = e^{2i\psi_{89}} \left[ (t_2^2 - 1) t_1^2 (-e^{2i\psi_{45}}) b_{Bs,12} - (t_1^2 - 1) e^{2i(\psi_{67} + \varphi)} b_{Bs,21} \right] + 2k_1 k_2 e^{i(\psi_{89} + \varphi)} (-t_2 + t_1 e^{i\psi} t_{Bs}) \quad (B7)$$

$$D = 1 + t_2 e^{i(\psi_{67} + \psi_{89})} \left[ t_2 t_1^2 e^{i(\psi_{45} + \psi)} (t_{Bs}^2 - b_{Bs,12}b_{Bs,21}) - 2k_1 k_2 e^{i(\psi_{67} + \varphi)} b_{Bs,21} - 2t_1 e^{i\psi_{45}} t_{Bs} \right] \quad (B8)$$

Below, to simplify the discussion we impose the following conditions on the position of the scatterer inside the ILMR:  $\psi_{89} = 2\psi_{45} = 2\psi_{67} = \psi/2$  ( $L_{89} = 2L_{45} = 2L_{67} = L/2$ ).

If the conditions describing a situation of "low" couplings ( $k_{1/2} \ll 1$ ,  $t_{1/2} \simeq 1$ ,  $|b_{Bs,12/21}| \ll 1$ ,  $t_{Bs} \simeq 1$ ,  $\sigma \simeq 1$ ) are met, and performing the following substitu-

tions:

$$t_{1/2} \simeq 1 - \frac{\Gamma_{L/R}}{\tilde{f}}, \quad k_{1/2} \simeq \sqrt{\frac{2\Gamma_{L/R}}{\tilde{f}}} \quad (\text{B9})$$

$$t_{Bs}\sigma \simeq 1 - \frac{\gamma}{\tilde{f}}, \quad \sigma := e^{-\alpha L} \quad (\text{B10})$$

$$\beta_{12} = 4e^{i\varphi} \sqrt{\Gamma_L \Gamma_R} \quad (\text{B11})$$

$$b_{Bs,12} \simeq \frac{\beta_{Bs,12}}{\tilde{f}}, \quad b_{Bs,21} \simeq \frac{\beta_{Bs,21}}{\tilde{f}} \quad (\text{B12})$$

$$\tilde{f} := \frac{c}{n_g L} = \frac{c \text{FSR}}{\lambda_0^2}, \quad \text{FSR} := \frac{\lambda_0^2}{n_g L} \quad (\text{B13})$$

$$\Re[\psi] = \frac{\Delta\omega}{\tilde{f}} \quad (\text{B14})$$

it is straightforward to verify that we get the same results derived through the Temporal Coupled Mode Theory (TCMT) equations reported in Eq. (1), Eq. (3), Eq. (6), and Eq. (7), namely:

$$\begin{aligned} \varepsilon_{\text{out,R}} = \varepsilon_{\text{in,L}} e^{i\varphi} & \left[ 1 + \right. \\ & - \frac{2\Gamma_R(-i\Delta\omega + \gamma_{\text{tot}}) + 2\Gamma_L(-i\Delta\omega + \gamma_{\text{tot}} - 4\Gamma_R)}{(-i\Delta\omega + \gamma_{\text{tot}})^2 - (\beta_{Bs,12} + 4e^{i\varphi} \sqrt{\Gamma_L \Gamma_R}) \beta_{Bs,21}} + \\ & + \left. \frac{2\sqrt{\Gamma_L \Gamma_R} (e^{-i\varphi} \beta_{Bs,12} + e^{i\varphi} \beta_{Bs,21})}{(-i\Delta\omega + \gamma_{\text{tot}})^2 - (\beta_{Bs,12} + 4e^{i\varphi} \sqrt{\Gamma_L \Gamma_R}) \beta_{Bs,21}} \right] \\ & + \varepsilon_{\text{in,R}} e^{i\phi} e^{i\varphi} \left[ \right. \\ & - \frac{4\sqrt{\Gamma_L \Gamma_R} (-i\Delta\omega + \gamma_{\text{tot}} - 2\Gamma_R)}{(-i\Delta\omega + \gamma_{\text{tot}})^2 - (\beta_{Bs,12} + 4e^{i\varphi} \sqrt{\Gamma_L \Gamma_R}) \beta_{Bs,21}} \\ & + \left. \frac{2e^{i\varphi} \Gamma_L \beta_{Bs,21} + 2e^{-i\varphi} \Gamma_R \beta_{Bs,12}}{(-i\Delta\omega + \gamma_{\text{tot}})^2 - (\beta_{Bs,12} + 4e^{i\varphi} \sqrt{\Gamma_L \Gamma_R}) \beta_{Bs,21}} \right] \quad (\text{B15}) \end{aligned}$$

$$\begin{aligned} \varepsilon_{\text{out,L}} = \varepsilon_{\text{in,R}} e^{i\phi} e^{i\varphi} & \left[ 1 + \right. \\ & - \frac{2\Gamma_R(-i\Delta\omega + \gamma_{\text{tot}}) + 2\Gamma_L(-i\Delta\omega + \gamma_{\text{tot}} - 4\Gamma_R)}{(-i\Delta\omega + \gamma_{\text{tot}})^2 - (\beta_{Bs,12} + 4e^{i\varphi} \sqrt{\Gamma_L \Gamma_R}) \beta_{Bs,21}} + \\ & + \left. \frac{2\sqrt{\Gamma_L \Gamma_R} (e^{-i\varphi} \beta_{Bs,12} + e^{i\varphi} \beta_{Bs,21})}{(-i\Delta\omega + \gamma_{\text{tot}})^2 - (\beta_{Bs,12} + 4e^{i\varphi} \sqrt{\Gamma_L \Gamma_R}) \beta_{Bs,21}} \right] \\ & + \varepsilon_{\text{in,L}} e^{i\varphi} \left[ \right. \\ & - \frac{4\sqrt{\Gamma_L \Gamma_R} (-i\Delta\omega + \gamma_{\text{tot}} - 2\Gamma_L)}{(-i\Delta\omega + \gamma_{\text{tot}})^2 - (\beta_{Bs,12} + 4e^{i\varphi} \sqrt{\Gamma_L \Gamma_R}) \beta_{Bs,21}} \\ & + \left. \frac{2e^{-i\varphi} \Gamma_L \beta_{Bs,12} + 2e^{i\varphi} \Gamma_R \beta_{Bs,21}}{(-i\Delta\omega + \gamma_{\text{tot}})^2 - (\beta_{Bs,12} + 4e^{i\varphi} \sqrt{\Gamma_L \Gamma_R}) \beta_{Bs,21}} \right] \quad (\text{B16}) \end{aligned}$$

In Eq. (B13)  $\tilde{f}$  is one over the cavity round-trip time.

In Eq. (B15) and Eq. (B16) it is observed that only if  $\beta_{Bs,12} \neq 0$  or/and  $\beta_{Bs,21} \neq 0$  the intensities depends on

$\varphi$ . Note that if one uses a symmetrical ILMR ( $\Gamma_L = \Gamma_R$ ) and assumes a Hermitian perturbation ( $\delta\beta = \beta_{Bs,12} = -\beta_{Bs,21}^*$ ), then the change of  $\varphi$  (rotation in the complex plane of  $\beta_{12}$ ) corresponds to a rotation of  $\delta\beta$  in the negative direction ( $e^{-i\varphi}$ ).

In conclusion, we have demonstrated that, if the following relations are satisfied ( $k_{1/2} \ll 1$ ,  $t_{1/2} \simeq 1$ ,  $|\beta_{Bs,12/21}| \ll 1$ ,  $t_{Bs}\sigma \simeq 1$ ) equivalent to ( $\Gamma_L \& \Gamma_R \& \gamma_{\text{tot}} \& |\beta_{12}| \& |\beta_{Bs,12}| \& |\beta_{Bs,21}| \ll \omega_0$ ), to move from a TCMT to a TMMs model one has to use the following relations:

$$\Gamma_{L/R} \simeq \tilde{f}(1 - t_{1/2}), \quad \Gamma_{L/R} \simeq \tilde{f} k_{1/2}^2 / 2 \quad (\text{B17})$$

$$\gamma \simeq \tilde{f}(1 - t_{Bs}\sigma), \quad \sigma := e^{-\alpha L} \quad (\text{B18})$$

$$\beta_{12} = 4e^{i\varphi} \sqrt{\Gamma_L \Gamma_R} \simeq 4e^{i\varphi} \tilde{f} \sqrt{(1 - t_1)(1 - t_2)} \quad (\text{B19})$$

$$\beta_{12} \simeq 2e^{i\varphi} \tilde{f} k_L k_R \quad (\text{B20})$$

$$\beta_{Bs,12} \simeq \tilde{f} b_{Bs,12}, \quad \beta_{Bs,21} \simeq \tilde{f} b_{Bs,21} \quad (\text{B21})$$

$$\tilde{f} := \frac{c}{n_g L} = \frac{c \text{FSR}}{\lambda_0^2}, \quad \text{FSR} := \frac{\lambda_0^2}{n_g L}. \quad (\text{B22})$$

### Appendix C: TCMT for the Taiji and the Ring microresonator

To generate Fig. 7 in Sec. IV, we used the TCMT equations for the Taiji and the microring resonator described below.

The TCMT equations that describe the Taiji are [36, 44]:

$$\begin{aligned} i \frac{d}{dt} \begin{pmatrix} \alpha_{\text{CCW}} \\ \alpha_{\text{CW}} \end{pmatrix} & = \begin{pmatrix} \omega_0 - i\gamma_{\text{tot,Taiji}} & -i(\beta_{12,\text{Taiji}} + \beta_{Bs,12}) \\ -i\beta_{Bs,21} & \omega_0 - i\gamma_{\text{tot,Taiji}} \end{pmatrix} \\ & \cdot \begin{pmatrix} \alpha_{\text{CCW}} \\ \alpha_{\text{CW}} \end{pmatrix} - \sqrt{2\Gamma_{\text{Taiji}}} \begin{pmatrix} E_{\text{in,L}} \\ E_{\text{in,R}} \end{pmatrix}, \quad (\text{C1}) \end{aligned}$$

$$\begin{pmatrix} E_{\text{out,R}} \\ E_{\text{out,L}} \end{pmatrix} = \begin{pmatrix} E_{\text{in,L}} \\ E_{\text{in,R}} \end{pmatrix} + i\sqrt{2\Gamma_{\text{Taiji}}} \begin{pmatrix} \alpha_{\text{CCW}} \\ \alpha_{\text{CW}} \end{pmatrix}. \quad (\text{C2})$$

Where  $\gamma_{\text{tot,Taiji}} = \gamma_{\text{Taiji}} + \Gamma_{\text{Taiji}} + 2\Gamma_S$  is the total loss rate of the Taiji microresonator composed by the propagation/absorption/scattering losses, the coupling losses with the bus waveguide and with the S-shaped waveguide, see Fig. 7 (b). Moreover, the coefficient  $\beta_{12,\text{Taiji}} = 4e^{i\varphi} \Gamma_S$ .

The TCMT equations that describe the Ring microresonator are [44]:

$$\begin{aligned} i \frac{d}{dt} \begin{pmatrix} \alpha_{\text{CCW}} \\ \alpha_{\text{CW}} \end{pmatrix} & = \begin{pmatrix} \omega_0 - i\gamma_{\text{tot, Ring}} & -i\beta_{Bs,12} \\ -i\beta_{Bs,21} & \omega_0 - i\gamma_{\text{tot, Ring}} \end{pmatrix} \\ & \cdot \begin{pmatrix} \alpha_{\text{CCW}} \\ \alpha_{\text{CW}} \end{pmatrix} - \sqrt{2\Gamma_{\text{Ring}}} \begin{pmatrix} E_{\text{in,L}} \\ E_{\text{in,R}} \end{pmatrix}, \quad (\text{C3}) \end{aligned}$$

$$\begin{pmatrix} E_{\text{out,R}} \\ E_{\text{out,L}} \end{pmatrix} = \begin{pmatrix} E_{\text{in,L}} \\ E_{\text{in,R}} \end{pmatrix} + i\sqrt{2\Gamma_{\text{Ring}}} \begin{pmatrix} \alpha_{\text{CCW}} \\ \alpha_{\text{CW}} \end{pmatrix}. \quad (\text{C4})$$

Where  $\gamma_{\text{tot, Ring}} = \gamma_{\text{Ring}} + \Gamma_{\text{Ring}}$  is the total loss rate of the Ring microresonator composed by the propagation/absorption/scattering losses and the coupling losses with the bus waveguide, see Fig. 7 (c).

## FUNDING

We acknowledge funding from PAT through the Q@TN joint lab, from Ministero dell'Istruzione, dell'Università e della Ricerca (PRIN PELM (20177 PSCKT)) and by European Union FSE-REACT-EU, PON Research and Innovation 2014–2020 DM1062/2021.

## ACKNOWLEDGMENTS

We gratefully thank Dr. Iacopo Carusotto for useful inputs and valuable comments. This work was supported by Q@TN, the joint lab between University of Trento, FBK- Fondazione Bruno Kessler, INFN- National Institute for Nuclear Physics and CNR- National Research Council. S.B. acknowledges the co-financing of the European Union FSE-REACT-EU, PON Research and Innovation 2014–2020 DM1062/2021.

## DISCLOSURES

The authors declare no conflicts of interest.

## DATA AVAILABILITY

Data underlying the results presented in this paper are not publicly available at this time but may be obtained from the authors upon reasonable request.

- 
- [1] Ramy El-Ganainy, Konstantinos G. Makris, Mercedeh Khajavikhan, Ziad H. Musslimani, Stefan Rotter, and Demetrios N. Christodoulides. Non-Hermitian physics and PT symmetry. *Nature Physics*, 14(1):11–19, January 2018. Number: 1 Publisher: Nature Publishing Group.
  - [2] Yuto Ashida, Zongping Gong, and Masahito Ueda. Non-Hermitian Physics. *Advances in Physics*, 69(3):249–435, July 2020. Number: 3 arXiv:2006.01837 [cond-mat, physics:quant-ph].
  - [3] Midya Parto, Yuzhou G. N. Liu, Babak Bahari, Mercedeh Khajavikhan, and Demetrios N. Christodoulides. Non-Hermitian and topological photonics: optics at an exceptional point. *Nanophotonics*, 10(1):403–423, January 2021. Publisher: De Gruyter.
  - [4] Hongfei Wang, Xiujian Zhang, Jinguo Hua, Danyuan Lei, Minghui Lu, and Yanfeng Chen. Topological physics of non-Hermitian optics and photonics: a review. *Journal of Optics*, 23(12):123001, December 2021.
  - [5] W. D. Heiss. Exceptional points of non-Hermitian operators. *Journal of Physics A: Mathematical and General*, 37(6):2455, January 2004.
  - [6] W. D. Heiss. The physics of exceptional points. *Journal of Physics A: Mathematical and Theoretical*, 45(44):444016, October 2012. Publisher: IOP Publishing.
  - [7] Dieter Heiss. Circling exceptional points. *Nature Physics*, 12(9):823–824, September 2016. Number: 9 Publisher: Nature Publishing Group.
  - [8] Jörg Doppler, Alexei A. Mailybaev, Julian Böhm, Ulrich Kuhl, Adrian Girschik, Florian Libisch, Thomas J. Milburn, Peter Rabl, Nimrod Moiseyev, and Stefan Rotter. Dynamically encircling an exceptional point for asymmetric mode switching. *Nature*, 537(7618):76–79, September 2016. Number: 7618 Publisher: Nature Publishing Group.
  - [9] Eric J. Pap, Daniël Boer, and Holger Waalkens. Non-Abelian nature of systems with multiple exceptional points. *Physical Review A*, 98(2):023818, August 2018. Number: 2.
  - [10] Xu-Lin Zhang, Tianshu Jiang, and C. T. Chan. Dynamically encircling an exceptional point in anti-parity-time symmetric systems: asymmetric mode switching for symmetry-broken modes. *Light: Science & Applications*, 8(1):88, October 2019. Number: 1 Publisher: Nature Publishing Group.
  - [11] Chong Chen, Liang Jin, and Ren-Bao Liu. Sensitivity of parameter estimation near the exceptional point of a non-Hermitian system. *New Journal of Physics*, 21(8):083002, August 2019. Number: 8.
  - [12] Jan Wiersig. Review of exceptional point-based sensors. *Photonics Research*, 8(9):1457, September 2020. Number: 9.
  - [13] Yulin Wu, Peiji Zhou, Ting Li, Weishi Wan, and Yi Zou. High-order exceptional point based optical sensor. *Optics Express*, 29(4):6080, February 2021.
  - [14] Emil J. Bergholtz, Jan Carl Budich, and Flore K. Kunst. Exceptional topology of non-Hermitian systems. *Reviews of Modern Physics*, 93(1):015005, February 2021. Publisher: American Physical Society.
  - [15] Haoye Qin, Xiaodong Shi, and Haiyan Ou. Exceptional points at bound states in the continuum in photonic integrated circuits. *Nanophotonics*, November 2022. Publisher: De Gruyter.
  - [16] Alexander Yulaev, Sangsik Kim, Qing Li, Daron A. Westly, Brian J. Roxworthy, Kartik Srinivasan, and Vladimir A. Aksyuk. Exceptional points in lossy media lead to deep polynomial wave penetration with spatially uniform power loss. *Nature Nanotechnology*, 17(6):583–589, June 2022. Number: 6.

- [17] Kenta Takata, Nathan Roberts, Akihiko Shinya, and Masaya Notomi. Imaginary couplings in non-Hermitian coupled-mode theory: Effects on exceptional points of optical resonators. *Physical Review A*, 105(1):013523, January 2022. Number: 1 arXiv:2107.08604 [physics].
- [18] Ran Huang, Ş. K. Özdemir, Jie-Qiao Liao, Fabrizio Minganti, Le-Man Kuang, Franco Nori, and Hui Jing. Exceptional Photon Blockade: Engineering Photon Blockade with Chiral Exceptional Points. *Laser & Photonics Reviews*, 16(7):2100430, 2022. Number: 7 eprint: <https://onlinelibrary.wiley.com/doi/pdf/10.1002/lpor.2021100430>.
- [19] Xiaoqian Shu, Aodong Li, Guangwei Hu, Jian Wang, Andrea Alù, and Lin Chen. Fast encirclement of an exceptional point for highly efficient and compact chiral mode converters. *Nature Communications*, 13(1):2123, April 2022. Number: 1 Publisher: Nature Publishing Group.
- [20] A. Hashemi, K. Busch, D. N. Christodoulides, S. K. Özdemir, and R. El-Ganainy. Linear response theory of open systems with exceptional points. *Nature Communications*, 13(1):3281, December 2022.
- [21] Weijian Chen, Şahin Kaya Özdemir, Guangming Zhao, Jan Wiersig, and Lan Yang. Exceptional points enhance sensing in an optical microcavity. *Nature*, 548(7666):192–196, August 2017. Number: 7666 Publisher: Nature Publishing Group.
- [22] Hossein Hodaei, Absar U. Hassan, Steffen Wittek, Hipolito Garcia-Gracia, Ramy El-Ganainy, Demetrios N. Christodoulides, and Mercedeh Khajavikhan. Enhanced sensitivity at higher-order exceptional points. *Nature*, 548(7666):187–191, August 2017. Number: 7666.
- [23] Jun-Hee Park, Abdoulaye Ndao, Wei Cai, Liyi Hsu, Ashok Kodigala, Thomas Lepetit, Yu-Hwa Lo, and Boubacar Kanté. Symmetry-breaking-induced plasmonic exceptional points and nanoscale sensing. *Nature Physics*, 16(4):462–468, April 2020. Number: 4 Publisher: Nature Publishing Group.
- [24] Alexander McDonald and Aashish A. Clerk. Exponentially-enhanced quantum sensing with non-Hermitian lattice dynamics. *Nature Communications*, 11(1):5382, December 2020. Number: 1.
- [25] Riccardo Franchi, Stefano Biasi, Filippo Mione, and Lorenzo Pavesi. On the response of the Taiji microresonator against small perturbation of the counter propagating mode. In Sonia M. García-Blanco and Pavel Cheben, editors, *Integrated Optics: Devices, Materials, and Technologies XXVI*, page 13, San Francisco, United States, March 2022. SPIE.
- [26] Bo Peng, Şahin Kaya Özdemir, Matthias Liertzer, Weijian Chen, Johannes Kramer, Huzeyfe Yılmaz, Jan Wiersig, Stefan Rotter, and Lan Yang. Chiral modes and directional lasing at exceptional points. *Proceedings of the National Academy of Sciences*, 113(25):6845–6850, June 2016. Publisher: Proceedings of the National Academy of Sciences.
- [27] L. Jin and Z. Song. Incident Direction Independent Wave Propagation and Unidirectional Lasing. *Physical Review Letters*, 121(7):073901, August 2018. Publisher: American Physical Society.
- [28] Jinhan Ren, Yuzhou G. N. Liu, Midya Parto, William E. Hayenga, Mohammad P. Hokmabadi, Demetrios N. Christodoulides, and Mercedeh Khajavikhan. Unidirectional light emission in PT-symmetric microring lasers. *Optics Express*, 26(21):27153, October 2018. Number: 21.
- [29] A. Muñoz de las Heras and I. Carusotto. Unidirectional lasing in nonlinear Taiji microring resonators. *Physical Review A*, 104(4):043501, October 2021. Publisher: American Physical Society.
- [30] Jing Zhang, Bo Peng, Şahin Kaya Özdemir, Kevin Pichler, Dmitry O. Krimer, Guangming Zhao, Franco Nori, Yu-xi Liu, Stefan Rotter, and Lan Yang. A phonon laser operating at an exceptional point. *Nature Photonics*, 12(8):479–484, August 2018. Number: 8 Publisher: Nature Publishing Group.
- [31] W.D. Heiss and H.L. Harney. The chirality of exceptional points. *The European Physical Journal D - Atomic, Molecular, Optical and Plasma Physics*, 17(2):149–151, November 2001.
- [32] C. Dembowski, B. Dietz, H.-D. Gräf, H. L. Harney, A. Heine, W. D. Heiss, and A. Richter. Observation of a Chiral State in a Microwave Cavity. *Physical Review Letters*, 90(3):034101, January 2003. Publisher: American Physical Society.
- [33] Changqing Wang, Xuefeng Jiang, Guangming Zhao, Mengzhen Zhang, Chia Wei Hsu, Bo Peng, A. Douglas Stone, Liang Jiang, and Lan Yang. Electromagnetically induced transparency at a chiral exceptional point. *Nature Physics*, 16(3):334–340, March 2020. Number: 3 Publisher: Nature Publishing Group.
- [34] S. Soleymani, Q. Zhong, M. Mokim, S. Rotter, R. El-Ganainy, and Ş. K. Özdemir. Chiral and degenerate perfect absorption on exceptional surfaces. *Nature Communications*, 13(1):599, February 2022. Number: 1 Publisher: Nature Publishing Group.
- [35] Junda Zhu, Changqing Wang, Can Tao, Zhoutian Fu, Haitao Liu, Fang Bo, Lan Yang, Guoquan Zhang, and Jingjun Xu. Imperfect chirality at exceptional points in optical whispering-gallery microcavities, August 2022. arXiv:2208.07077 [physics].
- [36] A. Calabrese, F. Ramiro-Manzano, H. M. Price, S. Biasi, M. Bernard, M. Ghulinyan, I. Carusotto, and L. Pavesi. Unidirectional reflection from an integrated “taiji” microresonator. *Photonics Research*, 8(8):1333, August 2020. Number: 8.
- [37] A. Guo, G. J. Salamo, D. Duchesne, R. Morandotti, M. Volatier-Ravat, V. Aimez, G. A. Siviloglou, and D. N. Christodoulides. Observation of  $\mathcal{PT}$ -Symmetry Breaking in Complex Optical Potentials. *Physical Review Letters*, 103(9):093902, August 2009. Publisher: American Physical Society.
- [38] Zin Lin, Hamidreza Ramezani, Toni Eichelkraut, Tsampikos Kottos, Hui Cao, and Demetrios N. Christodoulides. Unidirectional Invisibility Induced by  $\mathcal{PT}$ -Symmetric Periodic Structures. *Physical Review Letters*, 106(21):213901, May 2011. Publisher: American Physical Society.
- [39] Liang Feng, Xuefeng Zhu, Sui Yang, Hanyu Zhu, Peng Zhang, Xiaobo Yin, Yuan Wang, and Xiang Zhang. Demonstration of a large-scale optical exceptional point structure. *Optics Express*, 22(2):1760–1767, January 2014. Publisher: Optica Publishing Group.
- [40] H. Xu, D. Mason, Luyao Jiang, and J. G. E. Harris. Topological energy transfer in an optomechanical system with exceptional points. *Nature*, 537(7618):80–83, September 2016. Number: 7618 Publisher: Nature Publishing Group.

- [41] A. Muñoz de las Heras, R. Franchi, S. Biasi, M. Ghulinyan, L. Pavesi, and I. Carusotto. Nonlinearity-Induced Reciprocity Breaking in a Single Nonmagnetic Taiji Resonator. *Physical Review Applied*, 15(5):054044, May 2021. Number: 5.
- [42] Riccardo Franchi, Stefano Biasi, Alberto Muñoz de las Heras, Mher Ghulinyan, Iacopo Carusotto, and Lorenzo Pavesi. Influence of the bus waveguide on the linear and nonlinear response of a taiji microresonator. *Optics Express*, 29(19):29615, September 2021. Number: 19.
- [43] Dimitrios Chatzidimitriou, Alexandros Pitilakis, Trianos Yioultis, and Emmanouil E. Kriezis. Breaking Reciprocity in a non-Hermitian Photonic Coupler with Saturable Absorption. *Physical Review A*, 103(5):053503, May 2021. Number: 5 arXiv:2102.07483 [physics].
- [44] Stefano Biasi, Riccardo Franchi, Filippo Mione, and Lorenzo Pavesi. Interferometric method to estimate the eigenvalues of a non-Hermitian two-level optical system. *Photonics Research*, 10(4):1134, April 2022.
- [45] Changqing Wang, William R. Sweeney, A. Douglas Stone, and Lan Yang. Coherent perfect absorption at an exceptional point. *Science*, 373(6560):1261–1265, September 2021. Publisher: American Association for the Advancement of Science.
- [46] Stefano Biasi, Fernando Ramiro-Manzano, Fabio Turri, Pierre-Elie Larre, Mher Ghulinyan, Iacopo Carusotto, and Lorenzo Pavesi. Hermitian and Non-Hermitian Mode Coupling in a Microdisk Resonator Due to Stochastic Surface Roughness Scattering. *IEEE Photonics Journal*, 11(2):1–14, April 2019. Number: 2.
- [47] Qi Zhong, Mercedeh Khajavikhan, Demetrios N. Christodoulides, and Ramy El-Ganainy. Winding around non-Hermitian singularities. *Nature Communications*, 9(1):4808, November 2018. Number: 1 Publisher: Nature Publishing Group.
- [48] Ş K. Özdemir, S. Rotter, F. Nori, and L. Yang. Parity–time symmetry and exceptional points in photonics. *Nature Materials*, 18(8):783–798, August 2019. Number: 8 Publisher: Nature Publishing Group.
- [49] Stefano Biasi, Riccardo Franchi, and Lorenzo Pavesi. Interferometric cavity ringdown technique for ultrahigh Q-factor microresonators. *Optics Letters*, 47(16):4083–4086, August 2022. Number: 16 Publisher: Optica Publishing Group.
- [50] Bo Peng, Şahin Kaya Özdemir, Weijian Chen, Franco Nori, and Lan Yang. What is and what is not electromagnetically induced transparency in whispering-gallery microcavities. *Nature Communications*, 5(1):5082, December 2014.